



Influence of Input Parameters and Post-weld Heat Treatment on the Metallurgical and Mechanical Properties of Electron Beam-Welded Thick AISI 409 Ferritic Stainless Steel

Akash Doomra¹ · Beant Singh² · Sandeep Singh Sandhu³

Received: 24 October 2020 / Revised: 11 March 2021 / Accepted: 18 March 2021 / Published online: 12 April 2021
© ASM International 2021

Abstract

During this research work, the impact toughness and tensile strength of the electron beam-welded AISI409 plates were evaluated as a function of varied heat input (low 0.96 kJ/mm and high 1.10 kJ/mm) and after imparting post-weld heat treatment. Ferritic stainless steels are prone to enlargement in grain structure and degradation of mechanical properties on exposure to heating and cooling cycles during welding which results in deterioration in their performance. Results revealed that the base metal possessed coarse ferrite grains which got transferred into columnar and axial grains due to faster cooling rate of electron beam welding. The impact toughness of the specimens extracted from the top region of weld zone, when welded using high heat input, reduced by 46% as compared to the base metal. However, the specimens extracted from the bottom section possessed 83% higher impact toughness as compared to the top section. Further, the post-weld heat treatment resulted in refined microstructure, which increased the impact toughness by 35% and 24% for high heat input and low heat input welded joints, respectively. However, the tensile strength of the specimens extracted from the bottom section improved by 26% as compared to the base metal.

✉ Akash Doomra
er.doomra@gmail.com

Beant Singh
beantsingh7@yahoo.co.in

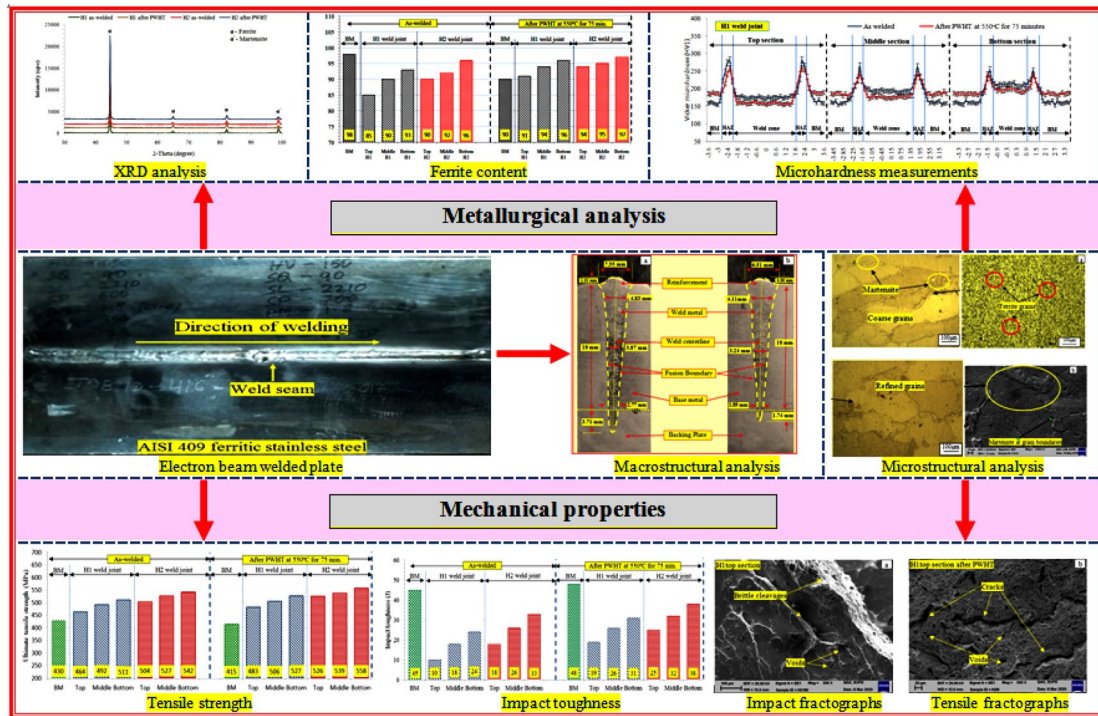
Sandeep Singh Sandhu
ersandeepsandhu@gmail.com

¹ Research Scholar, Department of Mechanical Engineering, IKG Punjab Technical University, Kapurthala, Punjab, India

² Department of Mechanical Engineering, Universal Group of Institutions, Lalru, Punjab 140501, India

³ Department of Mechanical Engineering, Quest Group of Institutions, Jhanjheri, Mohali 140307, Punjab, India

Graphical abstract



Keywords AISI 409 ferritic stainless steel · Electron beam welding · Mechanical properties · Metallurgical analysis · Fractography · Post-weld heat treatment

Introduction

Ferritic stainless steel (FSS) usually contains 10.5% to 30% chromium content and possesses BCC structure with a full ferritic microstructure at room temperature [1, 2]. They are relatively low-cost stainless steel alloys as compared to austenitic stainless steels, owing to their low nickel content [3]. They exhibit better mechanical strength than austenitic stainless steel and exhibit a low coefficient of thermal expansion and high thermal conductivity that makes it a better choice for applications that require thermal cycle resistance. They serve as a substitute to austenite steel in numerous applications especially the exhaust manifolds of an automobile. Ferritic stainless steels are categorized based on the chromium content they accommodate. Low-chromium ferritic stainless steel (10.5–13.5% Cr.) is found in applications such as automobile components, exhaust manifolds, and boilers, whereas medium chromium (14–18% Cr) and high chromium (20% or above) FSS are used in applications under aggressive environments such as petroleum industry, chemical industry, and electrical appliance [4–6]. AISI 409 FSS is low-chromium and low-carbon steel, and is popular due to its good corrosion resistance, low cost, and high heat

resistance. They are treated as an alternative to mild steels, low alloy steels, and coated steels that are used in applications under a corrosive environment. It is largely used in applications that are exposed to gasses at high temperatures such as mufflers, silencer, and exhaust tubing [7, 8].

Despite its great advantages and wide applicability in engineering applications, still, its expansion is limited owing to its post-weldability issues due to enlargements of grains in the weld zone [9]. FSS contains ferrite forming elements that enhance the formation of the ferrite phase during solidification and under certain conditions formation of martensite, chromium carbides, and nitrides were also observed. During the welding process, austenite is formed in the weld zone and heat-affected zone on achieving elevated temperature but upon rapid cooling, the formed austenite gets transformed into the martensite phase. Lippold and Kotecki [10] reported the formation of a fully ferritic structure or the combination of ferritic and martensite structure (where martensite sustains on the grain boundaries) during cooling of ferritic stainless steel. Further, to minimize the formation of martensite in WZ and HAZ, the carbon content is to be kept at the minimum level [11]. However, the presence of low-level martensite

is always favored as it helps to increase the toughness and also restrict grain growth [12]. Despite AISI409 is fairly weldable, still, the grains elongation in the WZ and HAZ attributes to degradation of impact and tensile strength of the welded joints [13, 14].

The mechanical properties of the FSS-welded joints are extremely dependent on the attained microstructure. Generally, the welding process parameters govern the types of microstructure that are formed. As addressed by various researchers [15–18] related to the issue of weldability, grain growth, and loss of mechanical properties during welding of FSS, it is suggested to employ low heat input welding techniques that result in refined grain structure and improved mechanical properties. High-end welding techniques such as electron beam welding and laser beam welding were suggested to be more favorable for welding ferritic stainless steel in comparison with conventional welding techniques such as GMAW, SMAW, and GTAW owing to their low heat input, high cooling rates, and ability to weld in a single pass [19]. Additionally, these welding processes work with a high-density beam that makes it feasible to attain a high-quality weld with relatively low heat and in small interaction time. The electron beam welding (EBW) process offers numerous advantages in comparison with other welding processes such as low heat input, high power density, deeper welds, low distortion, narrow WZ and HAZ, and minimum weld defect [20–23]. Cottrell [24] mentioned that EBW can be used to weld numerous grades of steel with the thickness of the plate up to 280 mm. Weglowski et al. [25, 26] discussed the various techniques and trends related to electron beam welding and mentioned that difficult to weld materials can be easily welded with high precision and improved mechanical properties. Lakshminarayanan et al. [27] made a comparison between electron beam-welded and friction stir-welded (FSW) of 4-mm-thick AISI409M FSS plates. The authors reported superior impact toughness and finer grain structure for the EBW process than the FSW process. Tullmin et al. [28] welded 6-mm-thick 40% Cr. FSS plate using an electron beam and laser beam welding process and compared the microstructural and impact properties. The electron beam-welded joint possessed higher impact toughness and the grain growth in the WZ and HAZ due to associated heat inputs were found to be minimum for both types of welded joints. Paul et al. [29] compared the microstructural characterization of 9% Cr ferritic martensite steel joints fabricated using an electron beam, laser beam, and tungsten inert gas welding process. The authors concluded that finer grains were observed in the case of the electron beam- and laser beam-welded joints, due to its high cooling rate and low heat input. Havlik et al. [30] investigated the properties of dissimilar welding between ferritic steel, martensite steel, and austenite steel using an electron beam welding process and reported that the formation of final microstructure after

solidification of weld pool solely depends upon its cooling rate.

Further, the application of post-weld heat treatment (PWHT) within the range of 550–850 °C [7] on ferritic stainless steel has been reported to be very advantageous by the various researchers [31–33]. A successfully implemented PWHT improves resistance to brittle fracture, and also improves the toughness and tensile strength of the welded joint as compared to the base metal. Anttila et al. [34] mentioned the refinement of grains and improvement in toughness and tensile strength after PWHT of the AISI409 weld joint fabricated using the GMAW process. Taban et al. [35] reported an improvement of 27% in impact toughness of PWHT specimens than the as-welded specimens of the 12% Cr. ferritic stainless steel weld joint fabricated using laser beam welding process.

Although several investigations have been made by various researchers on the electron beam welding of various grades of ferritic stainless steel, the data available on the effect of electron beam welding of AISI409 ferritic steel on metallurgical and mechanical properties are very scant. This study also addresses the effect of heat input on mechanical properties of 18-mm-thick AISI409 ferritic stainless steel-welded plate using an electron beam welding process. The present research work has been done with the intention of establishing the effect of heat input and investigating through-thickness variation of metallurgical and mechanical properties for 18-mm-thick EB-welded AISI409 ferritic stainless steel plates. Further, the correlation between the metallurgical and mechanical properties along the thickness has been established in as-welded state and after imparting post-weld heat treatment at 550 °C for 75 min is presented in this paper.

Experimental Procedure

AISI409 FSS plates with 18 mm thickness were used as a substrate. The chemical composition identified through spectro analysis in wt.% is 0.014 C, 0.390 Si, 0.582 Mn, 0.020 P, 0.007 S, 11.43 Cr., 0.33 Ni, 0.023 Mo, 0.015 Nb, 0.004 Ti and balance Fe. Two sets of plates were precisely machined to size 200 mm in length × 75 mm in width, with precisely machined edges at 90° to achieve a narrow gap butt joints. The plates were mechanically and chemically cleaned thoroughly to avoid any dust, chips, or unwanted particles.

The welded joints were prepared using an electron beam welding process after rigidly clamping the plates on the machine bed. The backing plate of the same material, i.e., AISI409 was fixed at the bottom of plates to avoid the flow of the molten weld pool. Prior to final welds, trial runs were conducted for the optimization of the welding process parameters. Fully penetrated square butt weld joints were

achieved with two levels of heat inputs (Table 1) in a single pass without any filler metal. To ensure the consistency and soundness of the weld joints, the plates were inspected by ultrasonic testing techniques and were found to be defect free.

Specimens Extractions

Specimens for metallographic analysis (microstructure, macrostructure, ferrite content, XRD, and microhardness) and mechanical testing (tensile test and impact test) were extracted from the welded plates with wire cut electro-discharge machining (EDM) as per the layout shown in Fig. 1. Two specimens were extracted in the direction transverse to the weld joint from each plate for metallographic analysis that comprises base metal (BM), heat-affected zone, and

weld zone. Two sets of subsized specimens perpendicular to the weld joints from the top, middle, and bottom sections were extracted for tensile strength test and impact toughness test as per ASTM standard E8 [36] and ASTM standard E23-12c [37], respectively, as shown in Fig. 1b and c.

Post-weld Heat Treatment

To enhance the microstructure and improve the mechanical properties of AISI409-welded joints, half of the extracted specimens from each of the plates were subjected to post-weld heat treatment at 550 °C for 75 min followed by furnace cooling till 500 °C and then by water quenching till room temperature is achieved. The time and temperature for PWHT were selected based on the literature survey conducted and to avoid the embrittlement phenomenon.

Metallographic Examination and Mechanical Testing

The specimens aimed for metallographic analysis were prepared as per ASTM standard E3-11 [38] which follows grinding, polishing with varying grit size emery paper (100–3000), and finally finishing with diamond paste. Microstructures were revealed by using Vilella reagent (5 ml HCL, 1 g picric acid, and 100 ml ethanol) as an etching agent for 25–30 s [39]. Examinations were conducted using an optical microscope coupled with a CCD camera at 100x. The identification of different phases in the weld zone was evaluated through the X-ray diffraction technique.

Table 1 Welding process parameters employed to achieve the welds

Parameters	Voltage Weld joint KV	Current mA	Speed mm/min	Heat Input kJ/mm
H1	150	90	700	1.10
H2	150	90	800	0.96

Gun to work distance = 447 mm, Root gap: < 0.25 mm, Oscillation frequency: 800 Hz, Beam oscillation amplitude: 1.8 mm, Gun vacuum: 2×10^6 mbar and chamber vacuum 5×10^6 mbar

Heat input calculation # Heat input per unit length of weld = $\eta (V \times I) / S$, whereas η denotes heat source efficiency (taken as 95%), V is beam voltage, I is beam current and S is beam travel speed

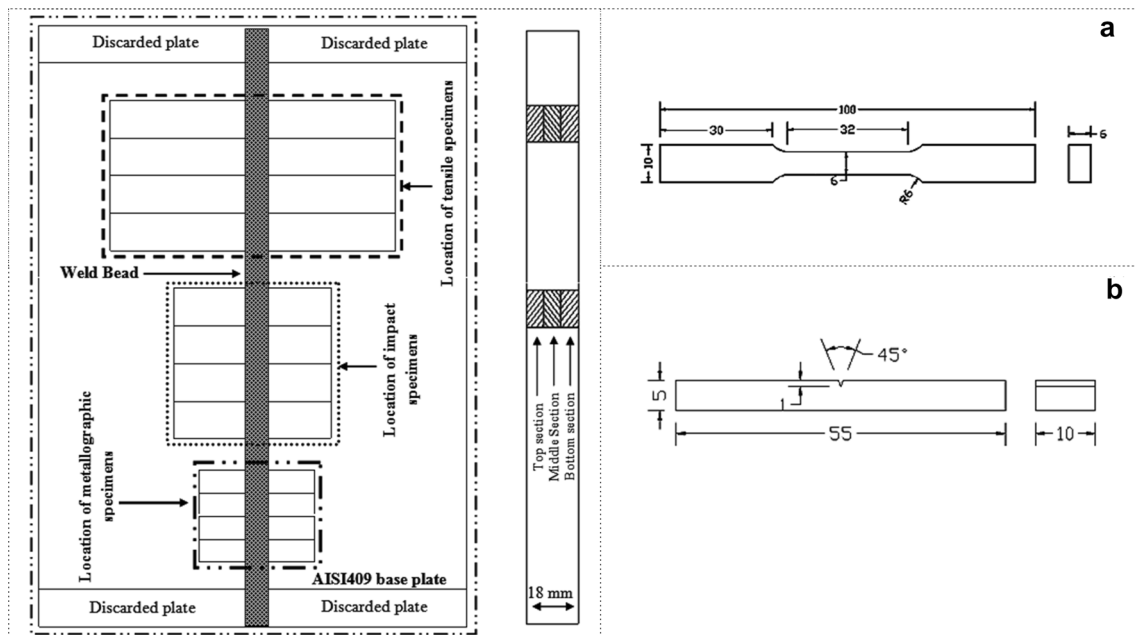


Fig. 1 (a) Specimens extraction plan from the welded plate, (b) Dimensions of specimen for tensile test, and (c) Dimensions of specimens for impact test

The average of 5 microhardness readings was taken along the weld centerline at a gap of 0.5 mm while traversing from the top to the bottom and across the weld centerline in a horizontal manner at a distance of 0.15 mm covering the base metal, HAZ, and weld zone at the top, middle and bottom sections of the weld bead. Readings were recorded on the metallurgical specimens using the Vicker microhardness testing machine at a load of 1 kg with a dwell time of 20 s. The ferrite content measurements were recorded using the Fisher ferritescope which estimates the amount of ferromagnetic content present.

The impact toughness tests were performed at room temperature using a pendulum-type Charpy V-notch impact testing machine. Notch was precisely machined along the weld centerline to avoid the variations in results. The room temperature transverse tensile tests were performed at a displacement rate of 4 mm/min using the Tinius Olsen testing machine. Further, the fracture behavior of the impact, and tensile specimens were examined under scanning electron microscopy.

Results and Discussion

Morphology of Weld Joints

The macrostructural weld profile (base metal, heat-affected zone, and weld zone) of AISI 409 FSS welded at two different heat inputs (H1 and H2) with electron beam welding including is shown in Fig. 2. Complete penetration throughout the thickness of the weld plate with geometrical consistency was achieved for both heat inputs. No excessive convexity, under cuts, underfills, etc. were observed in the fusion zone. The images confirm that the weld as a dagger-shaped, wider at the top region and narrow at the bottom region, was achieved due to the keyhole technique of the EBW process. The flow of the molten metal during the welding tends toward the parting line of WZ, which accumulates at the top of the weld joint as can be seen in Fig. 2. The flow of heat removal toward the side plate tends to elongate the grains perpendicular to the weld centerline. The transverse section of the image confirms adequate fusion of the substrate throughout the 18-mm-thick plates with no visible defect like porosity, cracks, volumetric defect, etc. The macrostructure of the joints fabricated at both the heat inputs favors the use of the EBW process for joining AISI 409 FSS in a single pass.

However, variations in morphologies were seen with the change in heat inputs during welding. For both the heat inputs, the width of penetration (top, middle, and bottom), depth of penetration (weld plate & backing plate), accumulation of weld pool at the top, and depth to width ratio were measured and are presented in Table 1. The results revealed

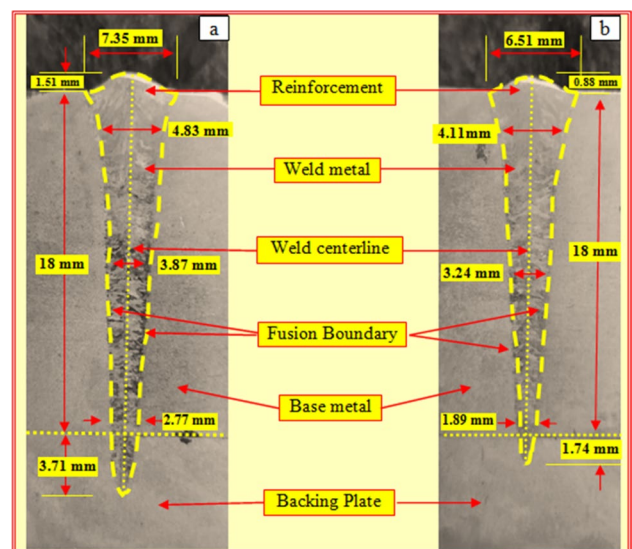


Fig. 2 Macrostructure image of (a) H1 weld joint and (b) H2 weld joints

smaller weld bead width and depth for H2 weld joints and that could be attributed to its lower heat input welding. The accumulated weld reinforcement at the top of the weld joint was also found smaller for low heat input parameters. This could be attributed to the formation of a lesser weld pool owing to its relatively lower heat input [40].

Microstructural Analysis

The microstructural investigations were carried out at magnification of 100× on the base plate and weld zone of the EBW joints in as-welded condition and after post-weld heat treated (PWHT) condition. Figure 3 displays the microstructure of AISI 409 ferritic stainless steel, typically exhibited equiaxed ferrite grain of approx 30 μm in diameter.

To predict the various phases developed in the weld zone during welding of AISI 409 FSS, Schaeffler diagram [2] was referred. The value of Chromium equivalent and Nickel equivalent was calculated using the equation as mentioned below.

$$Cr_{eq} = \%Cr + \%Mo + 1.5 \times \%Si + 0.5 \times \%Nb = 12.045 \quad (1)$$

$$Ni_{eq} = \%Ni + 30 \times \%C + 0.5 \times \%Mn = 1.041. \quad (2)$$

Chromium acts as a ferrite stabilizer whereas nickel acts as an austenite stabilizer. The ratio of Cr_{eq}/Ni_{eq} helps to understand the formation of the different phases in the weld zone. The increase in the Cr_{eq}/Ni_{eq} ratio increases the stability of the ferrite phase and decreases the stability of the austenite phase and the unstabilized austenite present gets transformed into the martensite [6]. The Schaeffler diagram

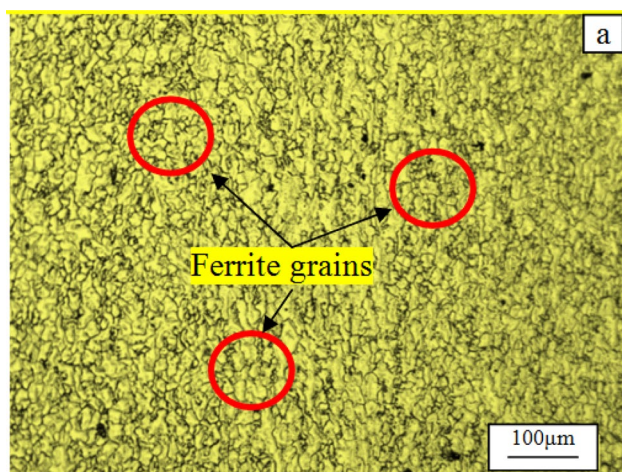


Fig. 3 Microstructure of AISI 409 FSS base metal

predicted the ferrite phase with a small amount of martensite as AISI 409FSS weld joints possess a high Cr_{eq}/Ni_{eq} ratio, i.e., 11.57. The microstructure analysis of both heat inputs reveals the formation of martensite at the grain boundaries of ferrite structure as can be seen in Figs. 4, 5, and 6. Further pseudo-binary phase diagram by Lippold and Savage [41] also predicted the formation of the primary ferrite phase during solidification of the weld zone, based on the Cr_{eq}/Ni_{eq} ratio.

Figures 4 and 5 represent the microstructure of top, middle, and bottom section of the weld joints made at two heat inputs H1 and H2. The weld zone mainly consists of large columnar grains at the outer portion and axial grains at the weld centerline. During the solidification of the weld pool, the maximum heats flow toward the sides of the weld zone owing to the temperature difference between the weld zone and plate edge, this leads to enlargement of grains in the direction perpendicular to the weld bead. The curved columnar grains are formed at the top reinforcement toward the sides (Fig. 4a) owing to the flow of heat to the sideways of the base plate as electron beam welding is performed in a vacuum chamber that reduces the flow of heat toward top of weld bead. Axial grains originated at the center of the weld bead elongates along the weld direction and these grains act as a hindrance to the columnar grains which originates from the fusion line. The axial grains are formed as these are last regions of the weld pool to solidify. This is similar as trends reported by various researchers [42, 43]. Figure 4a illustrates the microstructure at the weld centerline showing axial grains at the center and columnar grains elongated perpendicular to the weld centerline, whereas at the bottom section, the flow of heat is downward and sideways owing to the presence of a backing plate that acts as a thermal sink and this resulted in the grain growth toward the downside as can be clearly seen from Fig. 4h. The effect

of grain coarsening was observed throughout the thickness of the weld zone but a reduction in grain size was noticed while moving toward the bottom. Enlarged columnar grains were observed at the top section of the weld zone, which got reduced at the middle section. However, small columnar grains were observed at the bottom section for both the heat inputs. This through-thickness variation in grains structure while transversing from top to bottom may be attributed to the increased cooling rate, reduced heat input, and the presence of backing plate at the bottom. The keyhole mode of the welding technique reinforced the molten metal at the crown and narrowed at the root of the weld seam. The heat input was higher at the crown owing to its larger molten metal and lower at the root owing to the smaller width of the weld seam [21]. Heat input influences the cooling rate and significantly affects the microstructure of ferritic stainless steel [44]. The microstructure of H1 weld joints revealed higher coarsening and enlargement of grains with average grain of 263 μm in comparison with the H2 weld joint with average grain size of 196 μm , as relatively high heat input provides additional time for grains to elongate.

The microstructure of the weld zone also exhibits the presence of martensite at the ferrite grain boundaries for both the weld joints as can be seen from Figs. 4 and 5. The formation of different phases in the weld zone during solidification of the weld pool is mainly dependent on its cooling rate. The ferritic stainless steel always solidifies in single-phase ferrite and the transformation to austenite at elevated temperature and further transformation to martensite at low temperature is only through solid-state mode. However, during low heat input welding associated with the electron beam process, imparts lesser time for austenite phase to be stable which further leads to the formation of ferritic structure along-with island of martensite at the grain boundaries [40, 42]. In addition, AISI 409 FSS used in the present study does not contain a sufficient amount of austenite stabilizing elements thus causes the transformation to martensite in the weld zone. The comparison between the microstructure of both weld joints revealed a higher volume fraction of martensite for the H1 weld joint than the H2 weld joint. This may be attributed to the relatively low cooling rate of the H2 weld joint after welding associated with relatively high heat input. It is postulated that a lower cooling rate owing to high heat input during welding may exhilarate the transformation of ferrite to austenite, results in higher retained martensite content at room temperature [6]. Further, during through thickness analysis, the martensite was found to be reduced for the middle section and was least in the bottom section. Also, the presence of a high ferrite %age and low austenite %age at elevated temperatures restricted the formation of carbides in the structure.

Figure 6a and b displays the scanning electron microscopy image of the H1 weld zone at 500x and 1000x showing

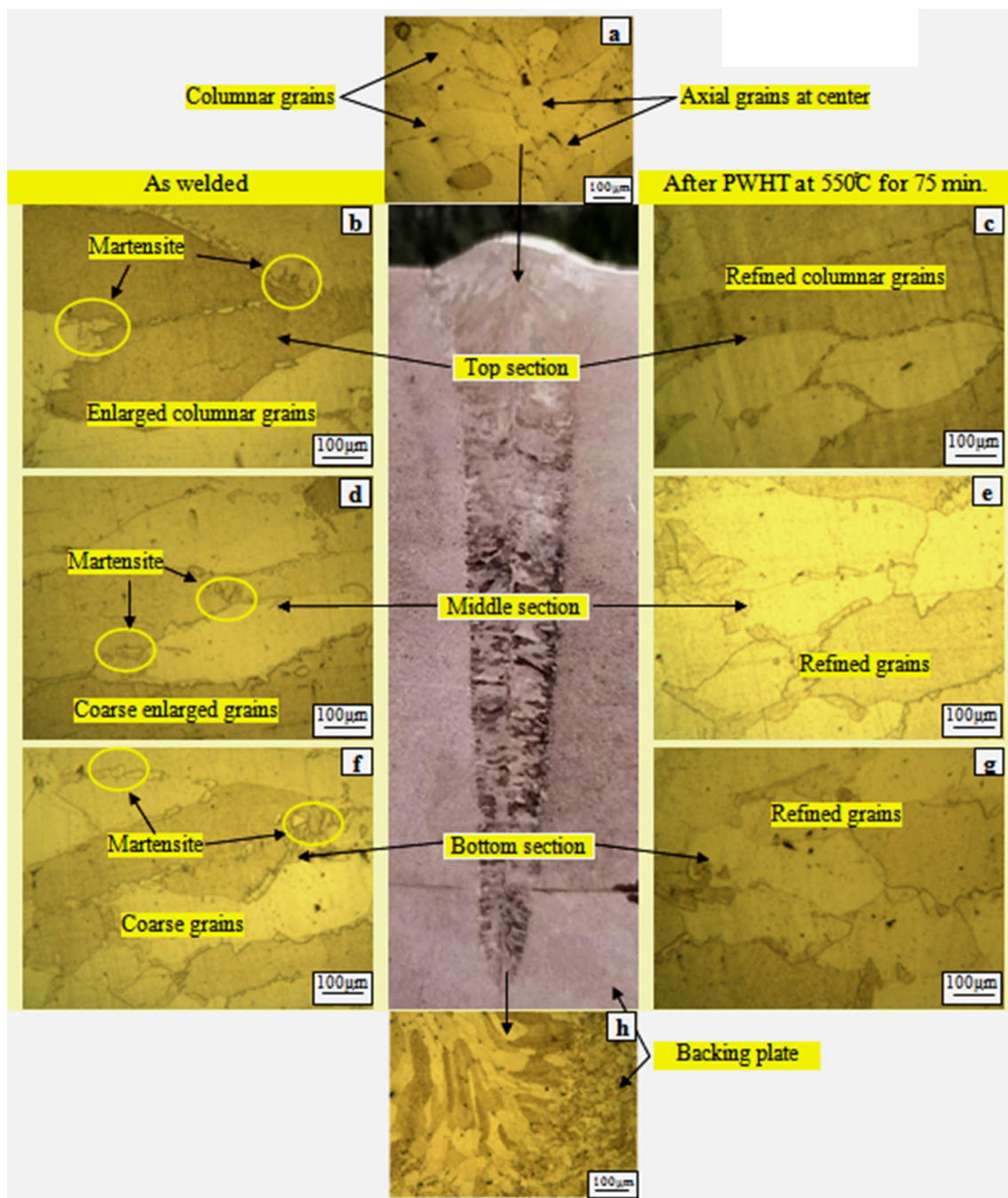


Fig. 4 Microstructure image of weld zone of H1 weld joint (a) top reinforcement, (b) top section as welded, (c) top section after PWHT, (d) middle section as welded, (e) middle section after PWHT, (f) bottom section as welded, (g) bottom section after PWHT and (h) backing plate

the formation of martensite islands at the grain boundaries of the ferrite.

Post-weld heat treatment at 550 °C for 75 min was conducted to refine the grain structure and temper the martensite in the weld zone. Figures 4c, e and g and 5b, d and f illustrate the microstructure of the weld joints H1 and H2 after PWHT, respectively. The coarse grains of the weld zone were transformed into refined grains. The volume fraction

of the martensite present at the ferrite grain boundaries was also decreased for all the weld joint specimens. That further attributed to the improvement in the impact toughness of the weld joint and also reduces the microhardness.

XRD characteristics were investigated for as-welded and PWHT specimens to identify the various phases formed and to reveal the formation of any carbide precipitation. XRD peaks for both the weld joints H1 and H2 are shown in Fig. 7. The

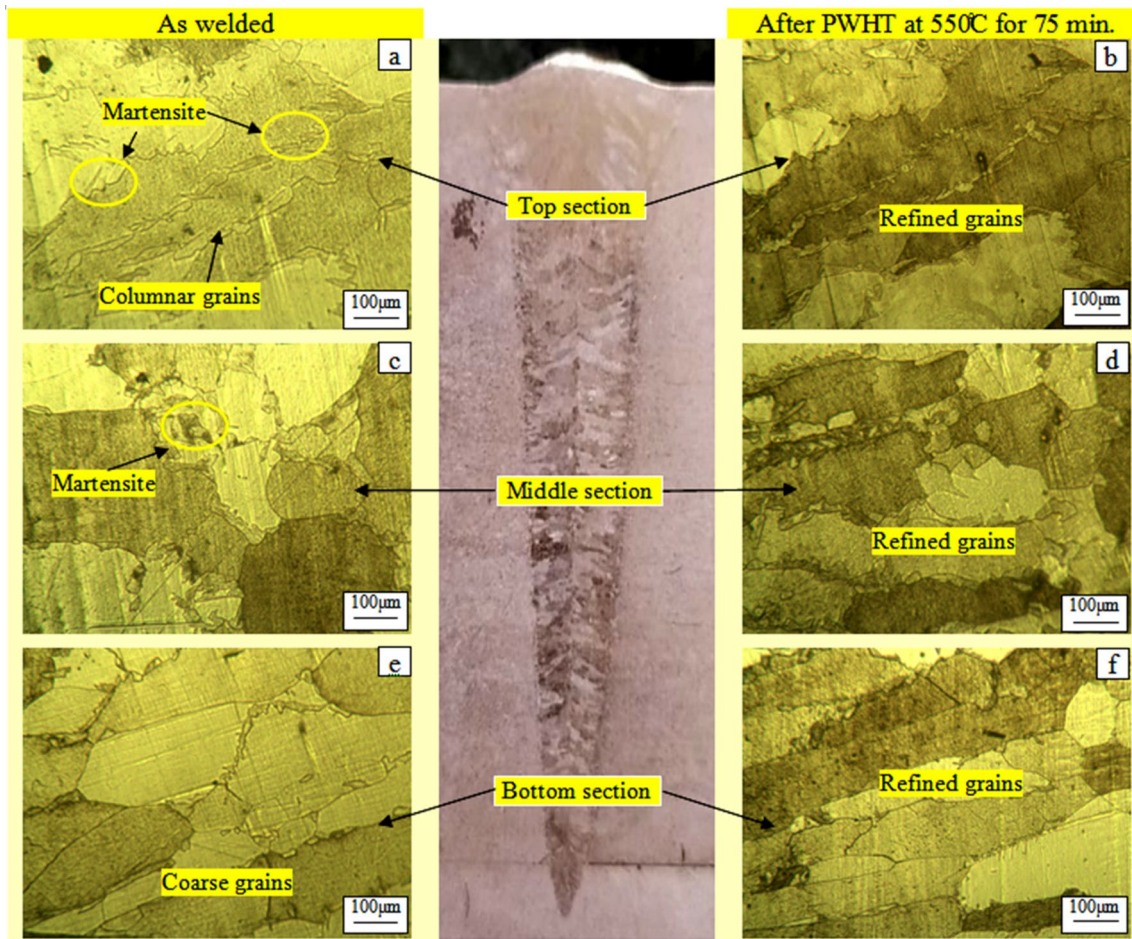


Fig. 5 Microstructure image of weld zone of H2 weld joint (a) top section as welded, (b) top section after PWHT, (c) middle section as welded, (d) middle section after PWHT, (e) bottom section as welded, and (f) bottom section after PWHT

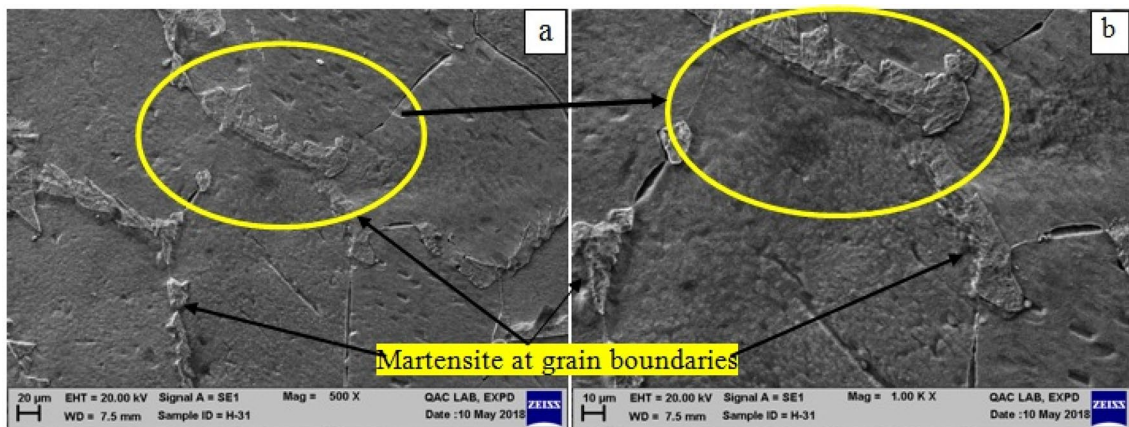
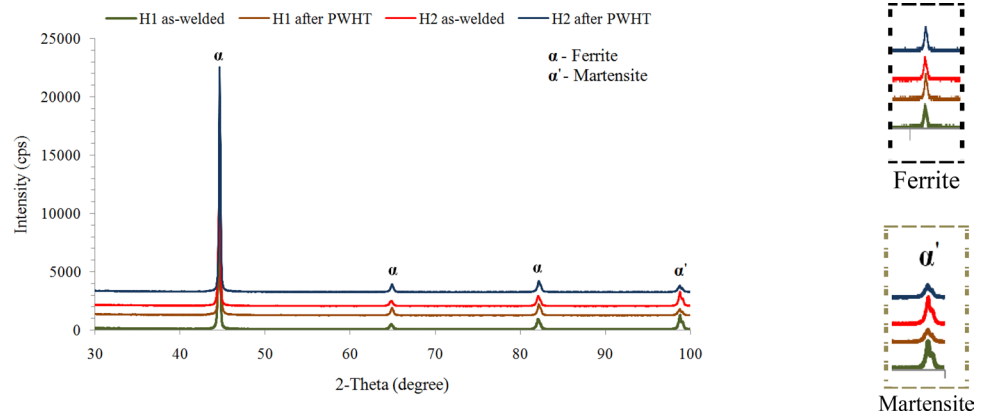


Fig. 6 Scanning electron microscopy images of weld zone (a) at 500X and (b) at 1000X

diffractograms indicate the presence of ferrite peaks and martensite peaks without any carbides or nitrides precipitates. Ferrite was the major phase in all the tested specimens along with

the small peak of martensite. Ferrite and martensite peaks are located at the same 2θ position but were distinguished by the peak width. Martensite peak width is broader than the ferrite

Fig. 7 X-ray diffraction pattern of H1 and H2 weld joints in as-welded and after PWHT condition



peaks as can be seen from Fig. 7b and c [45]. The ferrite peaks of the PWHT specimen were sharper than the as-welded specimen but the martensite peaks were small and wide.

Ferrite Content Variations

The ferrite content of the EB weld joint H1 and H2 was measured at the base metal and weld zone (top, middle, and bottom section) in as-welded and after PWHT using the Fisher ferritescope and the average results are graphically illustrated in Fig. 8. Since, the ferrite content of the weld zone is extremely influenced by its chemical composition, so new constituent diagram by Balmforth and Lippold [46] for solidified weld zone of ferrite-martensite steel was followed to predict the ferrite content. Cr_{eq} and Ni_{eq} were calculated using the below-mentioned equations

$$Cr_{eq} = Cr + 2Mo + 10(A + Ti) = 11.516 \tag{3}$$

$$Ni_{eq} = Ni + 35C + 20N = 0.82. \tag{4}$$

Tracing these values on the constitution diagram approximately 90% ferrite and 10% martensite content was predicted to be in the weld zone. The values measured with the ferritescope were found close to that of the predicted values. The ferrite content of the base metal in as-received condition was found to be 98% owing to its full ferrite structure but the PWHT reduces the ferrite content to 90%. The average ferrite content of the weld zone was reduced by 12% as compared to the base metal owing to the phase transformation of the weld zone during the welding process. On the comparison between the H1 and H2 weld joints, the average ferrite content of the H1 weld joint was found to be lesser than the H2 weld joint. The higher ferrite content of H2 weld joint could be ascribed to the rapid cooling rate relative to the H1 weld joint. While transversing from top to bottom of the weld zone, slight variation in ferrite content was seen throughout the thickness. The maximum value of ferrite

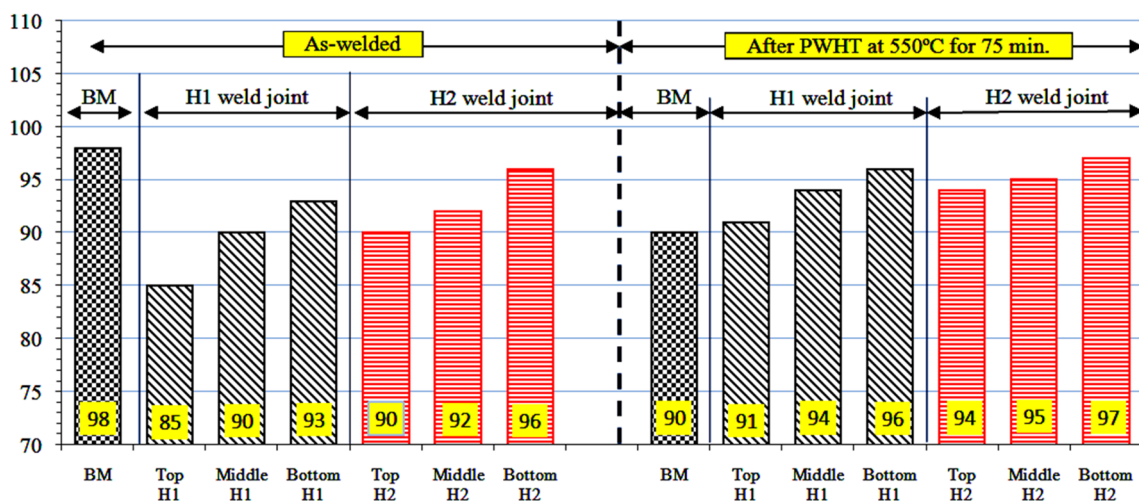


Fig. 8 Ferrite content variations of BM, H1 weld joint, and H2 weld joint at top, middle and bottom section in as-welded condition and after PWHT

content was observed at the bottom of the weld joint. The post-weld heat treatment at 550 °C for 75 min of the weld zone contributes to refine the grains structure and reduces the martensite phase from the weld zone that further results in rise of the ferrite content of the weld zone. Maximum rise in ferrite content after PWHT was observed at the top section and the minimum was observed at the bottom section of the weld zone. Further, the average ferrite content of the bottom section of H2 after PWHT was nearly equal to the base metal in as-welded condition.

Microhardness Variations

The microhardness evaluations (HV1/20 s) were carried along the weld centerline from top to bottom, and across the weld centerline covering base metal, heat-affected zone, and weld zone at the top, middle, and bottom section for both the welded joints. The average variations in microhardness captured are graphically depicted in Figs. 9 and 10. The base metal possessed the microhardness of 160HV1 whereas the WZ, and HAZ possessed higher microhardness throughout the weld seam. This could be attributed to a high-density electron beam welding process that associates rapid thermal cycles owing to its relatively low heat input [4]. The existence of the martensite phase in the HAZ and WZ of the AISI 409 ferritic stainless steel also plays an important role to increase the microhardness. Although for both the weld joints ferrite was transformed to martensite, microhardness in addition to martensite also depends upon the heat input [47]. Higher the heat input during welding possessed relatively lower microhardness of the weld joint. This is associated with the relatively smaller grains formed in the microstructure with relatively low heat input. In addition, the high heat input results in slow cooling rate which leads to enlarged grains in the weld zone, and further leads

to fall in the microhardness [48]. The average microhardness of high heat input weld joint H1 was recorded 192HV1 which was 10% lesser than the low heat input weld joint H2. Further, the top section of the weld zone for both of the weld joints possessed minimum microhardness, followed by the middle, and maximum at the bottom section. This could be attributed to relatively finer microstructure while transverse toward the bottom section, owing to smaller weld width at the bottom section contributed to a higher cooling rate. On the other hand, the HAZ showed the highest microhardness at the top section, which was 76% higher than the base metal, and 62% higher than the weld zone. This could be due to formation of martensite in the HAZ. Further, the microhardness of the HAZ of bottom section was reduced by 10% in comparison with the HAZ of the top section. The minimum microhardness of 172HV1 was recorded at the weld zone of the H1 top section, and the maximum microhardness of 239HV1 at the weld zone was recorded at the bottom section of the H2 joint.

Along the weld centerline microhardness for both the weld joints exhibited a slightly rising pattern while transverse from top to the bottom. The H2 weld joint exhibited maximum microhardness, i.e., 210HV1 at the top section, and 239HV1 at the bottom section (Fig. 10c). The increase of 13% in microhardness values from top to bottom could be due to the presence of a backing plate that acts as a thermal sink to absorb the heat, associated smaller weld pool, and lower heat input relative to the top section that promoted finer microstructure. Further, the PWHT at 550 °C for 75 min causes a substantial decrease in microhardness in WZ, and HAZ. The top section of the H1 weld joint experiences a maximum fall, i.e., 10% in microhardness. This could be attributed to the refinement of the grains structure, and tempering of the martensite present in the WZ, and HAZ. While, the

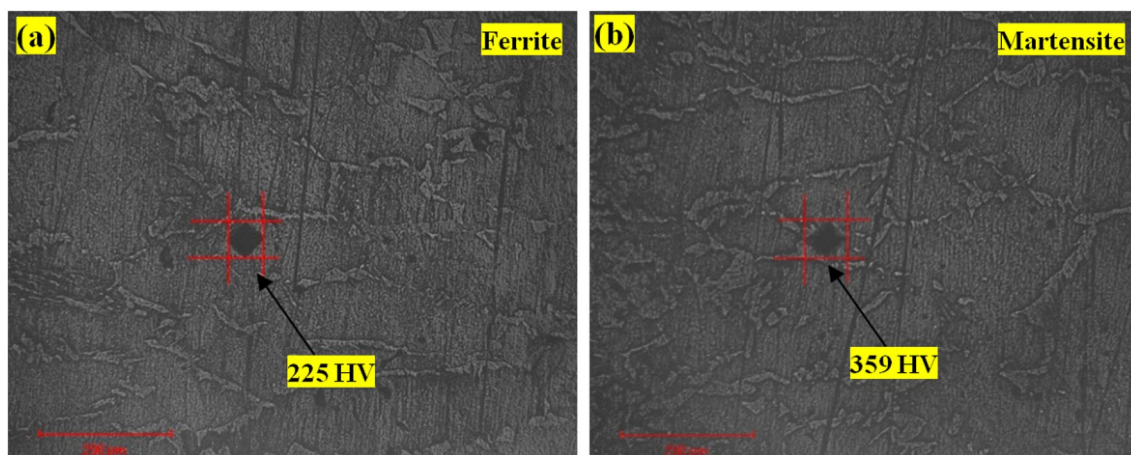


Fig. 9 Microhardness values of (a) Ferrite and (b) Martensite

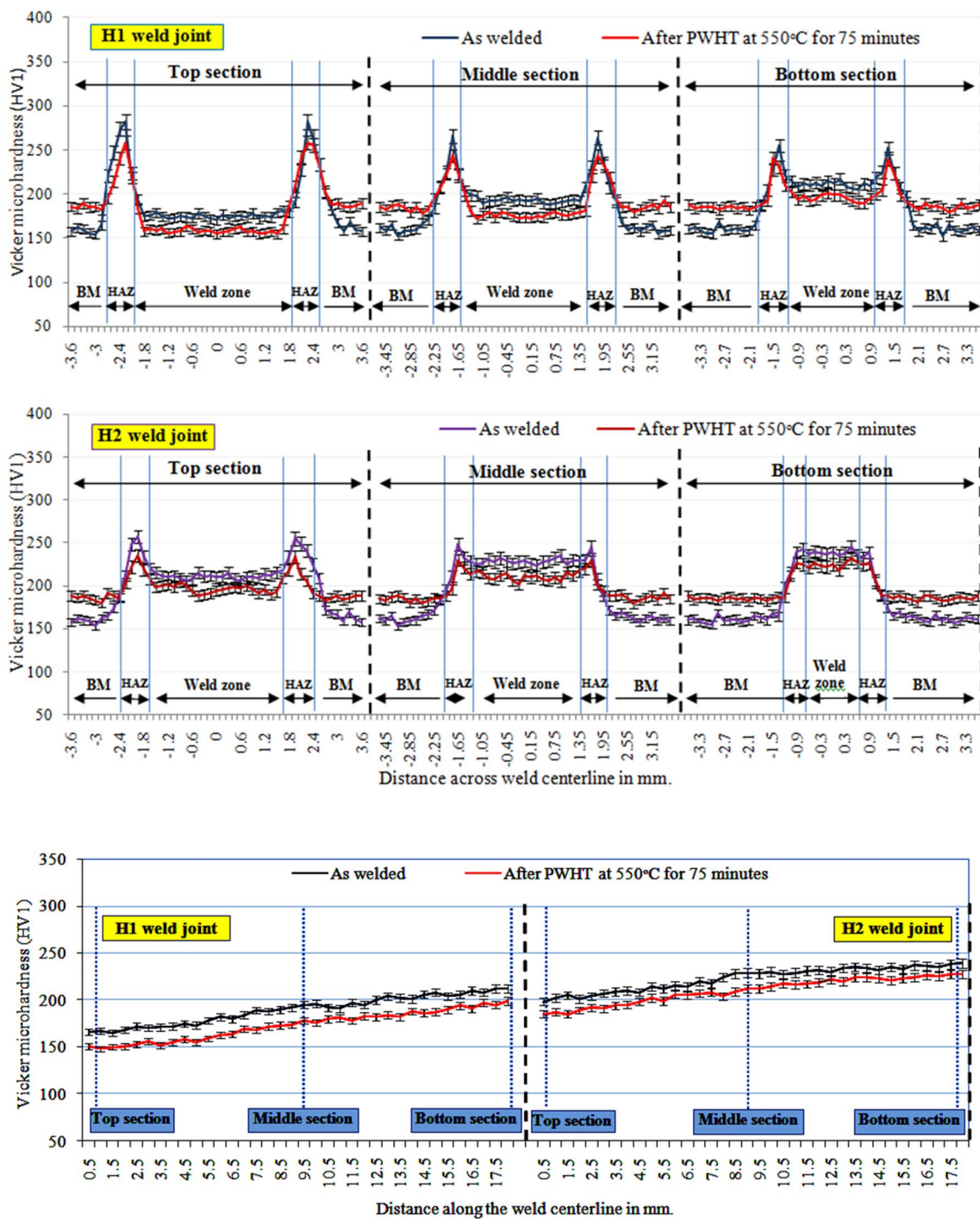


Fig. 10 Microhardness profile across the weld seam in as-welded condition and after PWHT for (a) H1 weld joint, (b) H2 weld joint, and (c) microhardness profile along the weld seam in as-welded condition and after PWHT

base metal exhibited a 16% rise in microhardness values after PWHT, owing to the formation of martensite at the grain boundaries, and decrease in the ferrite content. The microhardness readings were taken to identify the individual phases (ferrite and martensite phases) as shown in

Fig. 9, microhardness value at ferrite phase was recorded as 225 HV and on the martensite phase the reading was 359 HV.

Tensile Properties

The results obtained for the tensile test at room temperature for base metal, and top, middle, and bottom sections of both the weld joints (H1 & H2) are presented graphically in Figs. 11 and 12. The results were evaluated in terms of the ultimate tensile strength (UTS) and yield strength (YS) in as-welded condition and after PWHT at 550 °C for 75 min. The non-heat treated BM possessed the least UTS of 430 MPa and YS of 312 MPa among all the tested specimens. The results of the tested tensile specimens in as-welded conditions manifested agreement with the microhardness results. The base metal possessed least microhardness of 160HV1 as compared with the HAZ and WZ for both the heat inputs. The superior UTS and YS of the AISI 409 electron beam weld joints irrespective of the heat inputs may be attributed to the combination of the columnar and axial grains formed during solidification, rapid cooling rate, and formation of

martensite at the grain boundaries. All the tensile specimens fractured at the BM and the BM specimens fractured at the mid of gauge length. Despite the fact that all the tensile specimens fractured at the BM, even then the strength exhibited was different for different sections and heat inputs. This could be ascribed to the effect of thermal cycles at the area near HAZ that deviates the properties from as-received BM. Vidyarthi et al. [6] and Lakshminarayanan et al. [49] experienced identical behavior during the welding of FSS with different welding processes. The detrimental effect of the grain elongation and heat inputs were not experienced on the tensile properties of electron beam-welded joints. The H2 weld joints had higher UTS and YS as compared to H1 weld joints. The maximum UTS of 542 MPa and YS of 369 MPa were experienced at the bottom section of the H2 weld joints and minimum UTS of 464 MPa and YS of 315 MPa were experienced at the top section of the H1 weld joints. While analyzing along with the weld thickness

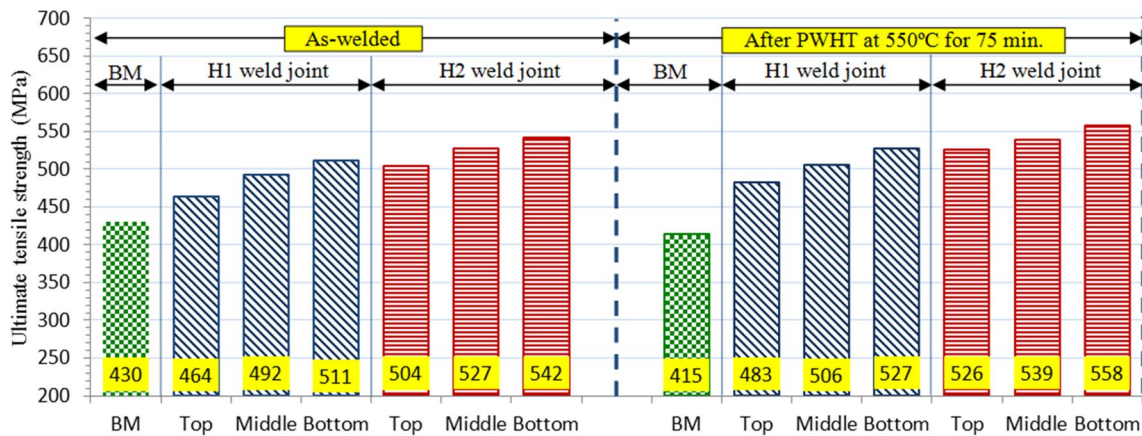


Fig. 11 Ultimate tensile strength variations of BM, H1 weld joint, and H2 weld joint at top, middle and bottom section in as-welded condition and after PWHT

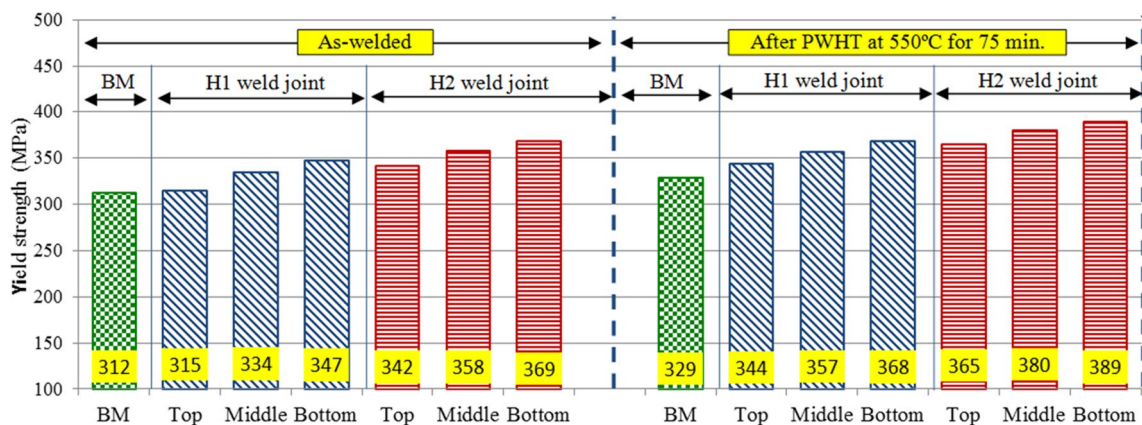


Fig. 12 Yield strength variations of BM, H1 weld joint, and H2 weld joint at top, middle and bottom section in as-welded condition and after PWHT

variations, increasing trends were experienced toward the bottom of the WZ with 464 MPa and 504 MPa at the top section, 492 MPa and 527 MPa at the middle section, and 511 MPa and 542 MPa at the bottom section for UTS of H1 and H2 weld joints, respectively. Similar behavior was experienced concerning to YS for both the weld joints. The relatively higher tensile properties at the bottom section resulted due to the comparatively refined microstructure and superior microhardness.

The PWHT of the weld zone gave incremental results in relation to tensile properties for both the heat inputs as clearly depicted in Figs. 11 and 12. Whereas the tensile properties of BM exhibited reduction after PWHT, this may be due to the coarsening of the grains due to thermal treatment. All the PWHT specimens got fractured from the BM regardless of the microhardness results. The microhardness of the PWHT top section and middle section of the H1 weld joint was lesser than the BM, still, the fracture occurred at BM. This may be attributed to the solidification structure attained by the weld pool and the existence of columnar and axial grains perpendicular to the crack propagation. These structures blunt the initiated crack tip and create a barrier to the advancement of the cracks. In order to propagate the cracks, the requirement of repeated force raises the essential mechanical energy that further improves the matrix strength [42]. Further, the improvement of tensile strength after PWHT is attributed to the refinement of the grain structure. The average UTS and YS after PWHT at 550 °C for 75 min were improved by 4% and 9%, respectively.

Impact Toughness of the Welds

The Charpy impact toughness was evaluated at room temperature in as-welded condition and after PWHT condition. The results attained for the BM and top, middle, and bottom section of H1 and H2 weld joints is graphically presented in Fig. 13. BM possessed the highest toughness of 45 J in

the as-received condition in comparison with all the tested specimens. The toughness of the AISI 409 FSS was found to be degraded after welding owing to the experienced thermal cycles. This deleterious effect is attributed to the microstructural changes such as grain elongation and martensite formation at the grains boundaries in the weld zone. High heat input H1 weld joint owing to its relatively coarse microstructure exhibited lower impact toughness than the H2 weld joint. This similar trend related to the reduction in toughness of FSS has been experienced by various researchers [6, 42, 48]. Further, the impact toughness was found to be improved for the bottom section as compared with the top and middle sections. The maximum impact toughness of 33 J was recorded for the H2 weld joint at the bottom section owing to its relatively smaller grain size and narrower weld zone. The PWHT of as-welded specimens significantly improved the impact toughness. The H1 weld joint was improved by 35% and the H2 weld joint was improved by 24%, respectively. The increase in the toughness of the weld joint could be attributed to the refinement of the grain structure and the tempering of the martensite. Further, the improved toughness was also found to be in agreement with the refinement of microstructure achieved after the PWHT. Fine grain structure reduces the stresses that emerged from piled-up dislocations and there-after enhances the impact toughness [48].

Fractography of Impact and Tensile Specimens

To reveal the fracture behavior of impact and tensile specimens, the fractured ends of specimens were analyzed using scanning electron microscopy. The final fractured behaviors were expressed by either brittle or combination of ductile and brittle behavior for all the specimens. Figures 14 and 15 manifest the fractographs of specimens which had least (top section of the H1 weld joint) and highest impact and tensile strength (bottom section of H2 weld joint) in as-welded condition and after PWHT condition. The top

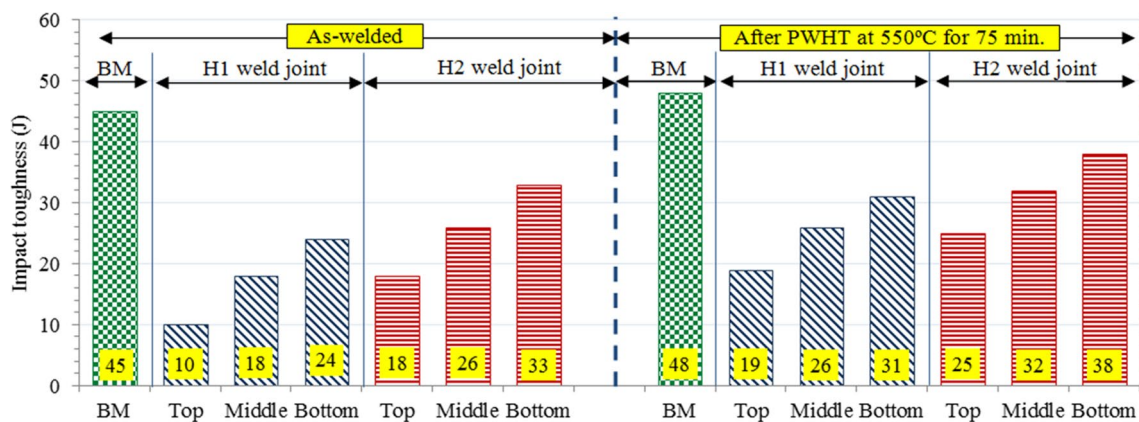


Fig. 13 Impact toughness of BM, H1, and H2 weld joint at top, middle and bottom section in as-welded condition and after PWHT

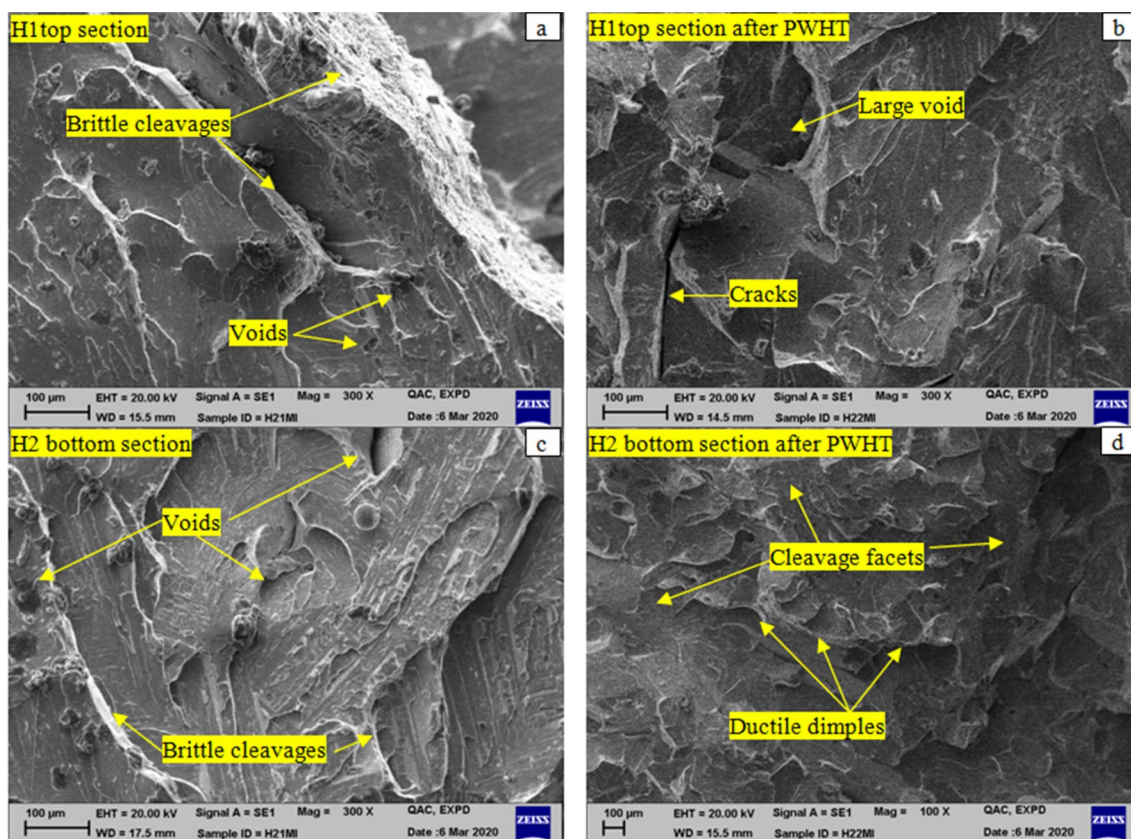


Fig. 14 Fractographs of impact tested specimens (a) top section of H1 weld joint in as-welded condition, (b) top section of H1 weld joint after PWHT condition, (c) bottom section of H2 weld joint in as-welded condition, and (d) bottom section of H2 weld joint after PWHT condition

section of H1 (Fig. 14a) exhibited brittle behavior with the presence of brittle cleavages, voids, and abrupt material removal. This might be the reason for the absorption of lower impact energy, whereas the bottom section of the H2 weld joint shown in Fig. 14c revealed the existence of scattered voids with less brittle cleavages. The presence of cleavage facets with a negligible amount of dimples were also evident. This fracture behavior forecasted higher impact toughness of the H2 bottom section as compared to the H1 top section.

The toughness of the EB weld joints was comparatively lower than the BM, so PWHT was carried out at 550 °C for 75 min. The fracture surface of PWHT impact specimens revealed the transformation of brittle fracture to a combination of ductile and brittle behavior, as displayed in Fig. 14b and d. H1 top section shows large voids, cracks, a large area of cleavage facets, minor ductile cleavages, and without the brittle cleavages that exhibit the transformation of the pure brittle behavior toward the ductile behavior. On the other hand, the H2 bottom section revealed few ductile dimples and cleavage facets with the absence of brittle cleavages. Heterogeneity in the dimples size was also recognized (Fig. 14d). This indicates

the improvement in impact toughness after PWHT and relatively had maximum impact toughness.

The fractured surfaces of the top section of the H1 weld joint under tensile loading exhibited brittle behavior. Some regions showed large cracks in addition to the voids and small cracks (Fig. 15a). The bottom section of the H2 weld joint (Fig. 15c) showed comparatively smaller cracks and voids along with minor ductile dimples this could be attributed to higher tensile strength than the top section of weld joint. Further, the PWHT of tensile specimen improved the fracture behavior mode by shifting from brittle mode to mixed mode of ductile and brittle behavior. The crack size and voids of H1 weld joints (Fig. 15b) were found to be reduced in addition to the ductile cleavage, whereas the H2 bottom section (Fig. 15d) exhibited a concentration of small dimpled rupture along with micro-voids and quasi cleavage. This might be attributed to better tensile properties.

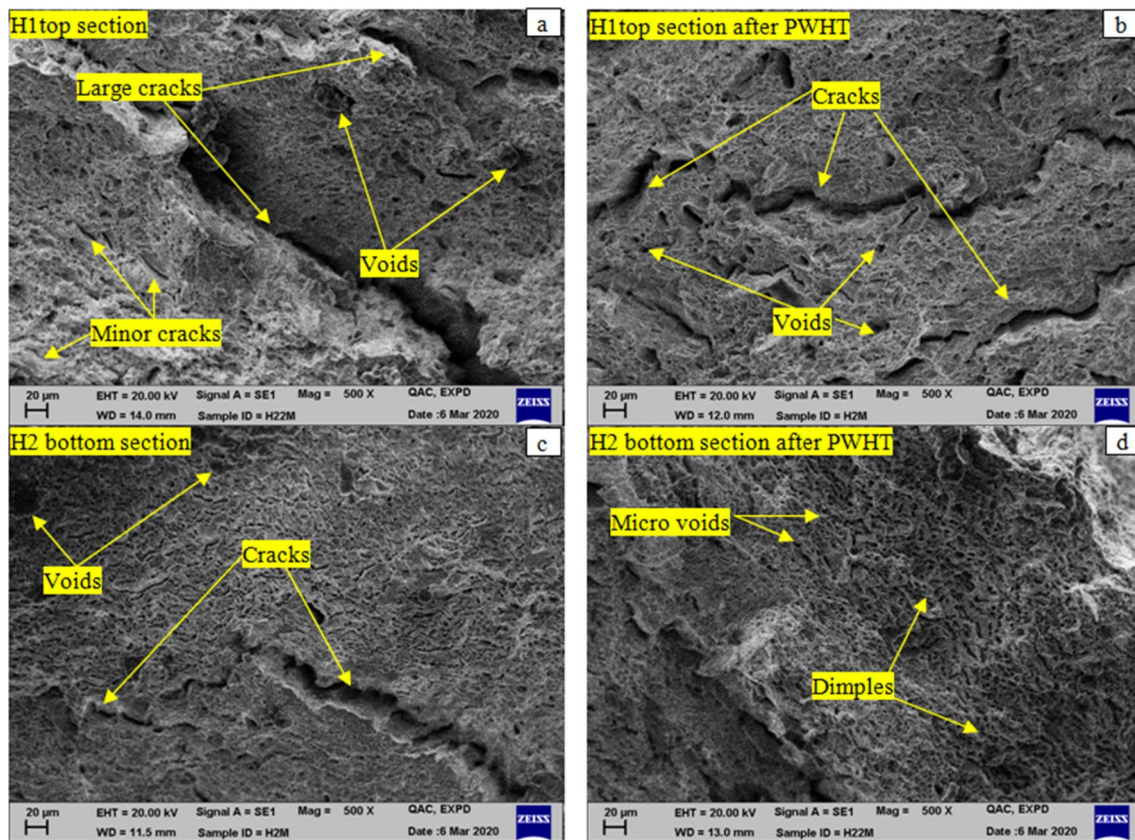


Fig. 15 Fractographs of tensile tested specimens (a) top section of H1 weld joint in as-welded condition, (b) top section of H1 weld joint after PWHT condition, (c) bottom section of H2 weld joint in as-welded condition, and (d) bottom section of H2 weld joint after PWHT condition

Conclusions

The present work investigated the effect of heat inputs and PWHT (550 °C/75 min) on metallurgical, impact, and tensile properties of electron beam-welded 18-mm-thick AISI 409 ferritic stainless steel. Based on the results, the below-mentioned conclusions can be drawn:

1. Fully penetrated AISI 409 ferritic stainless steel weld joints with adequate fusion were achieved in a single pass with both the heat inputs using electron beam welding process.
2. The weld zone of both the heat inputs consists of axial grains at the weld centerline and columnar grains toward the sideways. In addition, the weld zone of low heat input weld joint H1 exhibited relative fine-grained microstructure owing to its fast cooling rate.
3. Grain coarsening was observed throughout the thickness of the weld zone but a reduction in grain size was noticed while moving toward the bottom.
4. The heat-affected zone and weld zone of both the heat inputs exhibited relative higher microhardness than the base metal further the H2 weld joint possessed 10%

higher microhardness than the H1 weld joint owing to relatively less grain coarsening due to heat input.

5. The as-received BM possessed the least UTS of 430 MPa and YS of 312 MPa. Along the weld thickness, increasing trends were experienced toward the bottom of the WZ with 464 MPa and 504 MPa at the top section, 492 MPa and 527 MPa at the middle section, and 511 MPa and 542 MPa at the bottom section for UTS of H1 and H2 weld joints, respectively.
6. The PWHT of the weld zone enhanced the tensile properties by 4% approx. for both the heat inputs.
7. BM possessed the highest toughness of 45 J in the as-received condition. The maximum impact toughness of 33 J was recorded for the H2 weld joint at the bottom section. The PWHT of as-welded specimens significantly improved the impact toughness. The H1 weld joint was improved by 35% and the H2 weld joint was improved by 24%, respectively.

Acknowledgements The authors acknowledge the support and guidance provided by Mechanical Engineering Department, IK Gujral Punjab Technical University, Kapurthala.

References

- M.B. Cortie, History and development of ferritic stainless steels. *J. South. Afr. Inst. Min. Metall.* **93**(7), 165–176 (1993)
- D.J. Kotecki, T.A. Siewert, WRC-1992 constitution diagram for stainless steel weld metals: a modification of the WRC-1988 diagram. *Weld. Res. Suppl.* **71**(5), 171–178 (1992)
- E. Taban, A. Dhooge, E. Kaluc, Plasma arc welding of modified 12% Cr stainless steel. *Mater. Manuf. Process.* **24**(6), 649–656 (2009). <https://doi.org/10.1080/10426910902769152>
- C. Köse, C. Topal, Laser welding of AISI 410S ferritic stainless steel. *Mater. Res. Express* **6**(8), 1–14 (2019). <https://doi.org/10.1088/2053-1591/ab26c0>
- S.K. Gupta, A.R. Raja, M. Vashista, M.Z.K. Yusufzai, Effect of heat input on microstructure and mechanical properties in gas metal arc welding of ferritic stainless steel. *Mater. Res. Express* **6**(3), 1–46 (2018)
- R.S. Vidyarthi, D.K. Dwivedi, M. Vasudevan, Influence of M-TIG and A-TIG Welding Process on Microstructure and Mechanical Behavior of 409 Ferritic Stainless Steel. *J. Mater. Eng. Perform.* **26**(3), 1391–1403 (2017). <https://doi.org/10.1007/s11665-017-2538-5>
- C.J. Van Niekerk, M. Du Toit, M.W. Erwee, Sensitization of AISI 409 ferritic stainless steel during low heat input arc welding. *Weld. World* **56**, 55–64 (2012)
- M. Du Toit, C.J. Van Niekerk, Sensitization behaviour of 11–12% Cr AISI 409 stainless steel during low heat input welding. *J. South. African Inst. Min. Metall.* **111**(4), 243–256 (2011)
- A. Doomra, S.S. Sandhu, B. Singh, Weldability studies of 18 mm thick AISI409 ferritic stainless steel plate using electron beam welding process. *Int. J. Eng.* **18**(3), 23–28 (2020)
- J. C. Lippold and D. J. Kotecki, *Welding Metallurgy and Weldability of Stainless Steel*, vol. 21, No. 2, Wiley, 2006
- A.C.T.M. Van Zwieten, J.H. Bulloch, Some considerations on the toughness properties of ferritic stainless steels—A brief review. *Int. J. Press. Vessel. Pip.* **56**(1), 1–31 (1993). [https://doi.org/10.1016/0308-0161\(93\)90114-9](https://doi.org/10.1016/0308-0161(93)90114-9)
- M.O.H. Amuda, S. Mridha, An overview of sensitization dynamics in ferritic stainless steel welds. *Int. J. Corros.* **1–9**, 2011 (2011). <https://doi.org/10.1155/2011/305793>
- C. Grobler, Weldability Studies on 12% and 14% Chromium Steels, No. September, 1987
- E. Deleu, A. Dhooge, E. Taban, E. Kaluc, Possibilities and limitations to improve the weldability of low carbon 12Cr Ferritic stainless steel for expanded industrial applications. *Weld. World* **53**(9–10), 198–208 (2009). <https://doi.org/10.1007/BF03321131>
- M.A. Khattak et al., Effect of welding phenomenon on the microstructure and mechanical properties of ferritic stainless steel—a review *Akademia Baru. J. Adv. Res. Mater. Sci.* **1**(1), 13–31 (2017)
- A. Kumar, G. Sharma, D.K. Dwivedi, TIG spot weld bonding of 409 L ferritic stainless steel. *Int. J. Adhes. Adhes.* **84**, 350–359 (2018). <https://doi.org/10.1016/j.ijadhadh.2018.04.012>
- A. Doomra, S. S. Sandhu, and B. Singh, Effect of post weld heat treatment on metallurgical and mechanical properties of electron beam welded AISI 409 ferritic steel, 2020
- J.A. Delgado, R.R. Ambriz, R. Cuenca-Álvarez, N. Alatorre, F.F. Curiel, Heat input effect on the microstructural transformation and mechanical properties in GTAW welds of a409L ferritic stainless steel. *Rev. Metal.* (2016). <https://doi.org/10.3989/revmetalm.068>
- S.S. Sandhu, A.S. Shahi, Metallurgical, wear and fatigue performance of Inconel 625 weld claddings. *J. Mater. Process. Technol.* **233**, 1–8 (2016). <https://doi.org/10.1016/j.jmatprotec.2016.02.010>
- H. Schultz, *Electron Beam Technologies*, Vol. 1e. compact knowledge DVS media GmbH, Dusseldorf, 2012
- J. Singh, A.S. Shahi, Metallurgical, impact and fatigue performance of electron beam welded duplex stainless steel joints. *J. Mater. Process. Technol.* **272**, 137–148 (2019). <https://doi.org/10.1016/j.jmatprotec.2019.05.010>
- A. Kumar, S.S. Sandhu, B. Singh, Effect of thermal aging on impact toughness of electron beam-welded AISI 316 stainless steel. *Miner. Met. Mater. Ser.* (2020). https://doi.org/10.1007/978-3-030-36628-5_16
- A. Kumar, B. Singh, S.S. Sandhu, Effect of thermal aging on metallurgical, tensile and impact toughness performance of electron beam welded AISI 316 SS joints. *Fusion Eng. Des.* **159**(March), 111949 (2020). <https://doi.org/10.1016/j.fusengdes.2020.111949>
- C.L.M. Cottrell, Electron beam welding review—a critical. *Mater. Des.* **6**, 285–291 (1985)
- M.S. Węglowski, S. Błacha, A. Phillips, Electron beam welding—Techniques and trends—review. *Vacuum* **130**, 72–92 (2016). <https://doi.org/10.1016/J.VACUUM.2016.05.004>
- M. S. Węglowski, J. Dworak, and S. Błacha, *Electron Beam Welding – Characteristics*, no. 3, 2014
- A.K. Lakshminarayanan, V. Balasubramanian, Comparison of Electron Beam and Friction Stir Weldments of Modified 12 wt.% Ferritic Stainless Steel. *Mater. Manuf. Process.* **26**(6), 37–41 (2011). <https://doi.org/10.1080/10426914.2010.515643>
- M. Tullmin, F.P.A. Robinson, C.A.O. Henningt, A. Strausst, J. Le Grange, Properties of laser-welded and electron-beam-welded ferritic stainless steel. *J. South Afr. Inst. Min. Metall.* **89**(8), 243–249 (1989)
- V. Thomas Paul, S. Saroja, S.K. Albert, T. Jayakumar, E. Rajendra Kumar, Microstructural characterization of weld joints of 9Cr reduced activation ferritic martensitic steel fabricated by different joining methods. *Mater. Charact.* (2014). <https://doi.org/10.1016/j.matchar.2014.08.013>
- P. Havlík, P. Šohaj, J. Kouril, R. Foret, I. Dlouhý, EBW of Stainless Steels and ODS Ferritic Steel. *Methods* **4**, 5–6 (2014)
- M.O.H. Amuda, E. Akinlabi, S. Mridha, Ferritic stainless steels: metallurgy, application and weldability. *Ref. Modul. Mater. Sci. Mater. Eng.* (2016). <https://doi.org/10.1016/b978-0-12-803581-8.04010-8>
- M. Keskitalo, J. Sundqvist, K. Mäntyjärvi, J. Powell, A.F.H. Kaplan, The Influence of shielding gas and heat input on the mechanical properties of laser welds in ferritic stainless steel. *Phys. Procedia* **78**(August), 222–229 (2015). <https://doi.org/10.1016/j.phpro.2015.11.032>
- M.S. Rajadurai, S. Naveen, M. Afnas, T. Arun, N. Kumar, S. Surendhar, Methods to avoid material sensitization during welding for developing corrosion resistant exhaust system. *Int. J. Recent Dev. Eng. Technol.* **4**(7), 23–36 (2015)
- S. Anttila, P. Karjalainen, S. Lantto, Mechanical properties of ferritic stainless steel welds in using type 409 and 430 filler metals. *Weld. World* **57**(3), 335–347 (2013). <https://doi.org/10.1007/s40194-013-0033-7>
- E. Taban, E. Deleu, A. Dhooge, E. Kaluc, Laser welding of modified 12% Cr stainless steel: Strength, fatigue, toughness, microstructure and corrosion properties. *Mater. Des.* **30**(4), 1193–1200 (2009). <https://doi.org/10.1016/j.matdes.2008.06.030>
- ASTM Standard E8, Standard Test Methods for Tension Testing of Metallic Materials. *ASTM Int.* (2013). https://doi.org/10.1520/e0008_e0008m-13a
- ASTM standard E 23-12c, Standard Test Methods for Notched Bar Impact Testing of Metallic Materials. *ASTM Int.* (2013). <https://doi.org/10.1520/e0023-12c.2>
- ASTM standard E3-11, Standard Practice for Preparation of Metallographic Specimens. *ASTM Int.* **82**(C), 1–15 (2016). <https://doi.org/10.1520/d0638-14.1>
- ASTM Standard E407-99, E407-99: Standard Practice for Microetching Metals and Alloys, *ASTM Int.*, pp. 1–21, 2012

40. M.V. Venkatesan, N. Murugan, S. Sam, S.K. Albert, Effect of heat input on macro, micro and tensile properties of flux cored arc welded ferritic stainless steel joints. *Trans. Indian Inst. Met.* **67**(3), 375–383 (2014). <https://doi.org/10.1007/s12666-013-0358-3>
41. J. C. Lippold and W. F. Savage, Solidification of Austenitic Stainless Steel Weldments : Part I—A Proposed Mechanism The distribution and morphology of delta ferrite is dependent, *Weld. Res. Suppl.* No. December, pp. 362 s–374 s, 1979
42. A.K. Lakshminarayanan, V. Balasubramanian, G.M. Reddy, Microstructure and mechanical properties of electron beam-welded AISI 409 M-grade ferritic stainless steel. *Int. J. Adv. Manuf. Technol.* **1**, 153–162 (2011). <https://doi.org/10.1007/s00170-010-3044-1>
43. G.M. Reddy, K.S. Rao, Microstructure and mechanical properties of similar and dissimilar stainless steel electron beam and friction welds. *Int. J. Adv. Manuf. Technol.* (2009). <https://doi.org/10.1007/s00170-009-2019-6>
44. H. Zheng, X. Ye, L. Jiang, B. Wang, Z. Liu, G. Wang, Study on microstructure of low carbon 12% chromium stainless steel in high temperature heat-affected zone. *Mater. Des.* **31**(10), 4836–4841 (2010). <https://doi.org/10.1016/j.matdes.2010.05.054>
45. D.A. Carrizo, J.I. Besoky, M. Luppo, C. Danon, C.P. Ramos, Characterization of an ASTM A335 P91 ferritic-martensitic steel after continuous cooling cycles at moderate rates. *J. Mater. Res. Technol.* **8**(1), 923–934 (2019). <https://doi.org/10.1016/j.jmrt.2018.07.004>
46. M C Balmforth and J C Lippold, A New Ferritic-Martensitic Stainless Steel Constitution Diagram, *Weld. Res. Suppl.* No. December, pp. 339–345, 2000
47. J. Pekkarinen, V. Kujanpää, The effects of laser welding parameters on the microstructure of ferritic and duplex stainless steels welds. *Phys. Procedia* **5**(PART 1), 517–523 (2010). <https://doi.org/10.1016/j.phpro.2010.08.175>
48. V.L. Manugula, K.V. Rajulapati, G.M. Reddy, K.B.S. Rao, Role of evolving microstructure on the mechanical properties of electron beam welded ferritic-martensitic steel in the as-welded and post weld heat-treated states. *Mater. Sci. Eng., A* **698**, 36–45 (2017). <https://doi.org/10.1016/j.msea.2017.05.036>
49. A.K. Lakshminarayanan, V. Balasubramanian, Influences of welding processes on microstructure and mechanical properties of modified 12 wt.% Cr ferritic stainless steel. *Int. J. Manuf. Res.* **7**(4), 331–353 (2012). <https://doi.org/10.1504/IJMR.2012.050100>

Publisher's Note Springer Nature remains neutral with regard to jurisdictional claims in published maps and institutional affiliations.